Available online at www.sciencedirect.com
SCIENCE DIRECT®
Journal of Solid State Chemistry 177 (2004) 2777–2782
JOURNAL OF SOLID STATE CHEMISTRY
http://elsevier.com/locate/jssc

Synthesis, structure and VUV luminescent properties of rubidium rare-earth fluorides

Fangtian You,[a,*] Shihua Huang,[a] Shuman Liu,[a] and Ye Tao[b]

[a] *Laboratory of Materials for Information Storage and Display, Institute of Optoelectronic Technology, Beijing Jiaotong University, Beijing 100044, China*

[b] *Beijing Synchrotron Radiation Laboratory, Institute of High Energy Physics, Beijing 100039, China*

Received 11 December 2003; received in revised form 12 April 2004; accepted 19 April 2004

Abstract

RbF–LnF$_3$ (Ln = rare earth) systems were synthesized by hydrothermal technique. Under the hydrothermal condition, the light rare-earth elements form LnF$_3$ (Ln= La−Nd), while the heavy ones form RbLn_2F$_7$ (Ln = Y, Er, Yb and Lu) with the RbEr$_2$F$_7$ structure type. RbLn_3F$_{10}$ compounds were found for the in-between rare-earth cations (Ln= Eu−Tm and Y), which crystallize exclusively in the cubic γ-KYb$_3$F$_{10}$-type structure. The luminescent properties under vacuum ultraviolet light were studied for the Eu^{3+}-doped RbLn_3F$_{10}$ (Ln = Y, Gd) and a high quantum efficiency of about 150% was observed for RbGd$_3$F$_{10}$:Eu^{3+}.

Keywords: Rubidium rare-earth fluorides; Hydrothermal synthesis; Vacuum ultraviolet (VUV); Energy transfer; Quantum cutting effect

1. Introduction

The specific optical characteristic of fluoride materials is their large band gap and low phonon energy, which lead to lower multiphonon relaxation rates and high luminescence efficiencies. The energy transfer of rare-earth ions in fluorinated host matrices is of particular importance as far as the emission efficiency of vacuum ultraviolet (VUV) phosphors is concerned [1]. Recently, Wegh et al. [2] demonstrated that in the Eu^{3+}-doped LiGdF$_4$ the excitation energy was transferred via a two-step process from Gd^{3+} to Eu^{3+}, resulting in two visible emission photons. The quantum efficiency might approach to 200%. Their work shows us a new class of phosphors, i.e., visible quantum cutting phosphors, which seem promising for application in mercury-free fluorescent tubes and in plasma display panels.

Rubidium and rare-earth fluoride systems have been studied extensively. The phases obtained by solid-state reactions at high temperature include Rb$_3Ln$F$_6$, Rb$_2Ln$F$_5$, RbLnF$_4$, RbLn_2F$_7$ and RbLn_3F$_{10}$ [3]. It is generally accepted that the formation and the structure of complex fluorides depend strongly on cation sizes. Thoma et al. [4] rationalized the formation of alkaline and rare-earth fluorides by $R = r_{M^+}/r_{Ln^{3+}}$, and Vedrine et al. [5] further pointed out that the cubic RbLn_3F$_{10}$ compounds were formed only in a narrow range $1.41 < R < 1.49$ in the RbF–LnF$_3$ system. The dependence of the structure type of MLn_3F$_{10}$ on the ionic radii of rare earths has also been studied by Kang et al. [6]. RbLn_3F$_{10}$ is known to have several different structure types: the γ-KYb$_3$F$_{10}$ structure, β-KYb$_3$F$_{10}$ structure and CsYb$_3$F$_{10}$ structure [3]. For example, RbGd$_3$F$_{10}$ has two crystalline structures: α-RbGd$_3$F$_{10}$ and β-RbGd$_3$F$_{10}$. α-RbGd$_3$F$_{10}$ [7] is isostructural with γ-KYb$_3$F$_{10}$ that crystallizes in a fluorite-related crystal structure. The structure consists of two different units [KYb$_3$F$_8$] and [KYb$_3$F$_{12}$], which alternate along the three crystallographic axes. β-RbGd$_3$F$_{10}$ [8] crystallizes in the β-KYb$_3$F$_{10}$ structure in the space group $P6_3mc$, in which the rare-earth atoms are coordinated by eight fluorine atoms in a bicapped trigonal prismatic geometry. The CsYb$_3$F$_{10}$ [9] structure type features for the large alkaline metal cations and, the rare-earth cations are coordinated in a pentagonal bipyramidal geometry.

*Corresponding author. Fax: +861051688018.
E-mail address: ftyou@center.njtu.edu.cn (F. You).

0022-4596/$ - see front matter © 2004 Elsevier Inc. All rights reserved.
doi:10.1016/j.jssc.2004.04.040

Another phase in the RbF–LnF_3 system $RbLn_2F_7$ also has three different structure types, i.e., a disordered fluorite-type (Ln= La−Gd) [10], KEr_2F_7-type (Ln= Sm, Gd, Dy and Yb) [11] and $RbEr_2F_7$-type (Ln= Eu, Gd, Dy, Er and Y) [12]. The UV and visible luminescent properties have been studied for some of these complex rubidium fluorides, such as β-$RbGd_3F_{10}$ [8], $RbGd_3F_{10}$:Eu^{2+} [7], $RbGd_3F_{10}$:Eu^{3+} [13] and RbY_2F_7:Gd^{3+} [14], but their VUV luminescent properties were rarely discussed.

The complex fluorides were conventionally synthesized by solid-state reaction at high temperature. Such reaction, however, requires complicated setup and corrosive HF gas to avoid contamination from oxygen. Recently, it was reported that oxygen-free complex fluorides could be prepared by hydrothermal synthesis [15]. We introduced this method in the synthesis of $NaGdF_4$ [16] and a series of fluorides $NH_4Ln_3F_{10}$ (Ln= Dy, Ho, Y, Er, Tm) [6]. Considering the similar ionic radii between Rb^+ and NH_4^+, we carried out a systematic study on hydrothermal synthesis of the RbF–LnF_3 system. In this paper, we present the synthesis and VUV luminescence properties of these rubidium and rare-earth fluorides.

2. Experimental

The starting materials were Rb_2CO_3 (A.R.), RbF (A.R.), Ln_2O_3 (99.99%) and HF (A.R.). Table 1 lists the reaction conditions for $RbGd_3F_{10}$. For a typical synthesis, the starting materials were mixed with the following mol ratio: $3.0Rb_2CO_3$:$3.0Gd_2O_3$:20.0HF:100-H_2O, the reactant mixture was sealed in a Teflon-lined stainless steel autoclave and heated at 220°C for 5 days. After the autoclaves were cooled and depressurized, the product was washed with deionized water and dried in air at ambient temperature. Similar hydrothermal reactions were applied to the other rare-earth systems (Ln= La, Pr, Nd, Sm, Eu, Tb, Dy, Ho, Er, Tm, Yb, Lu and Y), and the optimized condition was also applied to the synthesis of Eu^{3+}-doped samples with starting mol ratio of $3.0Rb_2CO_3$:$3.0(1-x)Ln_2O_3$:$3.0xEu_2O_3$:20.0HF:$100H_2O$ ($x = 0.5$ mol%).

The products were characterized by X-ray powder diffraction recorded on a Rigaku D/max-2400 powder diffractometer with Cu$K\alpha$ radiation. The excitation and emission spectra were measured on the Spectroscopy Station of Beijing Synchrotron Laboratory. The excitation spectra, detected by an EMI9635QB PMT, were calibrated using sodium salicylate as a standard.

3. Results and discussion

3.1. Hydrothermal synthesis and structure of RbF–LnF_3 system

To optimize conditions, the hydrothermal reaction of $RbGd_3F_{10}$ was studied systematically as shown in Table 1. Both Rb_2CO_3 and RbF have been used as reacting substances and it seems that the rubidium source does not influence the result of the reaction. The critical factors for obtaining the single-phase product are the pH value, the initial composition and the reaction temperature. The single-phase product of $RbGd_3F_{10}$ could be obtained in the pH range 2–6. Lower pH favors the formation of GdF_3; while higher pH value often results in the presence of $Gd(OH)_3$. The ratio of Rb/Gd also affects the products. $RbGd_3F_{10}$ is formed when the Rb/Gd ratio is over 2/3, and a larger ratio is favorable for crystallization, so excess amount of Rb_2CO_3 was employed in order to adjust the pH value and improve the crystallization. The hydrothermal reaction may

Table 1
Synthesis reactions and products in the hydrothermal syntheses of $RbGd_3F_{10}$

Starting materials			$a:b:c$ mole ratio	pH[a]	Temp. (°C)	Time (days)	Phases in product
a	b	c					
Rb_2CO_3	Gd_2O_3	HF	3:3:20	3/5	220	4	$RbGd_3F_{10}$
RbF	Gd_2O_3	HF	6:3:20	3/5	220	4	$RbGd_3F_{10}$
Rb_2CO_3	Gd_2O_3	HF	1:3:20	1/3	220	4	GdF_3 + $RbGd_3F_{10}$
Rb_2CO_3	Gd_2O_3	HF	2:3:20	2/4	220	4	$RbGd_3F_{10}$
Rb_2CO_3	Gd_2O_3	HF	6:3:20	4/6	220	4	$RbGd_3F_{10}$
Rb_2CO_3	Gd_2O_3	HF	9:3:20	5/6	220	4	$RbGd_3F_{10}$
Rb_2CO_3	Gd_2O_3	HF	3:3:40	1/2	220	4	GdF_3
Rb_2CO_3	Gd_2O_3	HF	30:3:20	8/10	220	4	$RbGd_3F_{10}$ + $Gd(OH)_3$
Rb_2CO_3	Gd_2O_3	HF	3:3:20	3/5	220	8	$RbGd_3F_{10}$
Rb_2CO_3	Gd_2O_3	HF	3:3:20	3/5	220	2	$RbGd_3F_{10}$
Rb_2CO_3	Gd_2O_3	HF	3:3:20	3/5	220	1	$RbGd_3F_{10}$
Rb_2CO_3	Gd_2O_3	HF	3:3:20	3/5	180	4	$RbGd_3F_{10}$
Rb_2CO_3	Gd_2O_3	HF	3:3:20	3/5	140	4	$RbGd_3F_{10}$ + Gd_2O_3
Rb_2CO_3	Gd_2O_3	HF	3:3:20	3/5	140	12	$RbGd_3F_{10}$

[a] Both initial and final pH values are given.

complete within 1 day at 220°C, but 12 days were required at 140°C, indicating that the transformation from oxide to fluoride is a slow process at low temperature. The synthetic reaction for the preparation of $RbGd_3F_{10}$ is expressed as:

$$Rb_2CO_3+3Gd_2O_3+20HF = 2RbGd_3F_{10}+CO_2 +10H_2O, \quad (1)$$

$$2RbF + 3Gd_2O_3+18HF = 2RbGd_3F_{10}+9H_2O. \quad (2)$$

Under above hydrothermal conditions, one could only obtain the cubic α-$RbGd_3F_{10}$ phase, and no hexagonal β-$RbGd_3F_{10}$ was found. Fig. 1 shows the X-ray powder diffraction pattern of the product, and the lattice constant of the cubic α-$RbGd_3F_{10}$ is $a = 11.796$ Å.

The systematic study on $RbGd_3F_{10}$ demonstrates that hydrothermal technique is a promising method for the syntheses of rubidium rare-earth fluorides. Therefore, the optimized hydrothermal condition of the synthesis of $RbGd_3F_{10}$ was applied to the other RbF–LnF$_3$ systems (Ln= La, Pr, Nd, Sm, Eu, Tb, Dy, Ho, Er, Tm, Yb, Lu and Y). Table 2 lists the products obtained by hydrothermal reactions. It was found that the light rare earths (Ln= La, Pr and Nd) only form rare-earth fluorides LnF_3. For the Sm system, the product was a mixture of SmF_3 and $RbSm_2F_7$, which might be the decomposed products of $RbSm_3F_{10}$ [5]. The in-between rare earths (Ln= Eu−Tm and Y) form RbLn_3F_{10} in the γ-KYb_3F_{10}-type cubic structure. The lattice constants listed in Table 2 decrease with the ionic radii of the rare-earth cations. For the smaller rare-earth cations (Ln= Y, Er, Yb and Lu), RbLn_2F_7 was formed under the hydrothermal conditions:

$$Rb_2CO_3+2Y_2O_3+14HF = 2RbY_2F_7+CO_2+7H_2O. \quad (3)$$

RbLn_2F_7 (Ln= Y, Er, Yb and Lu) obtained in this study all crystallize in the hexagonal $RbEr_2F_7$ structure type. Fig. 2 shows the X-ray powder diffraction patterns of RbY_2F_7 and RbY_3F_{10}, and the refined lattice parameters are listed in Table 2.

Unlike the solid-state reaction at high temperature, the stoichiometry of the product, in general, is not controllable by the ratio of the starting materials in hydrothermal reaction. The product of the hydrothermal reaction, however, may depend on the equilibrium in the solution and the stability relative to the other possible phases. In our study, only three kinds of compounds, tetragonal LnF_3, cubic RbLn_3F_{10} and hexagonal RbLn_2F_7 were found. Nevertheless, it seems that the compounds formed under the hydrothermal condition exhibit correlation to the cation sizes ($R = r_M + /r_{Ln}3+$), which can be clearly seen from the data shown in Table 3. The large rare-earth cations with $R<1.42$ (Ln= La to Nd) only form simple rare-earth trifluorides LnF_3. The cubic RbLn_3F_{10} was obtained for the in-between rare-earth cations (Ln= Sm−Tm and Y)

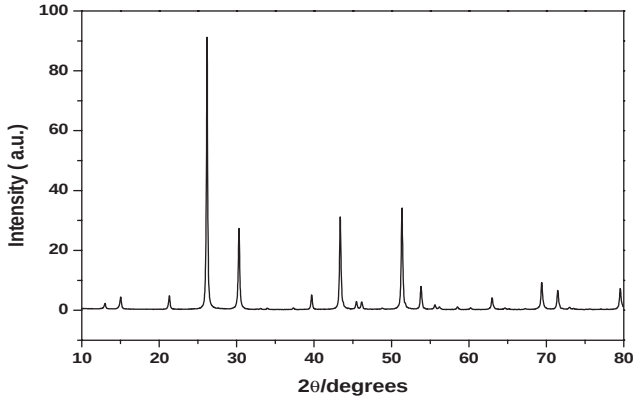

Fig. 1. X-ray powder diffraction pattern of $RbGd_3F_{10}$.

Table 2
The structure parameters of the products obtained by hydrothermal syntheses for the Rb–Ln–F systems

System	Product	Crystal system	Lattice parameters (Å)	
			Calculated	In literature
La	LaF_3	Tetragonal	$a = 7.186$, $c = 7.351$	$a = 7.186$, $c = 7.350$ [3]
Pr	PrF_3	Tetragonal	$a = 7.072$, $c = 7.235$	$a = 7.078$, $c = 7.237$ [3]
Nd	NdF_3	Tetragonal	$a = 7.028$, $c = 7.197$	$a = 7.029$, $c = 7.196$ [3]
Sm	$SmF_3 + RbSm_2F_7$			$a = 11.954$ [4]
Eu	$RbEu_3F_{10}$	Cubic	$a = 11.812$	$a = 11.844$ [4,10]
Gd	$RbGd_3F_{10}$	Cubic	$a = 11.796$	$a = 11.828$ [4,11]
Tb	$RbTb_3F_{10}$	Cubic	$a = 11.721$	$a = 11.787$ [4]
Dy	$RbDy_3F_{10}$	Cubic	$a = 11.667$	
Ho	$RbHo_3F_{10}$	Cubic	$a = 11.614$	
Y	RbY_3F_{10}	Cubic	$a = 11.593$	
	RbY_2F_7	Hexagonal	$a = 15.532$, $c = 11.983$	$a = 15.521$, $c = 11.978$ [15]
Er	$RbEr_3F_{10}$	Cubic	$a = 11.554$	
	$RbEr_2F_7$	Hexagonal	$a = 15.510$, $c = 11.964$	$a = 15.586$, $c = 11.968$ [3]
Tm	$RbTm_3F_{10}$	Cubic	$a = 11.509$	
Yb	$RbYb_2F_7$	Hexagonal	$a = 15.380$, $c = 11.880$	
Lu	$RbLu_2F_7$	Hexagonal	$a = 15.329$, $c = 11.860$	

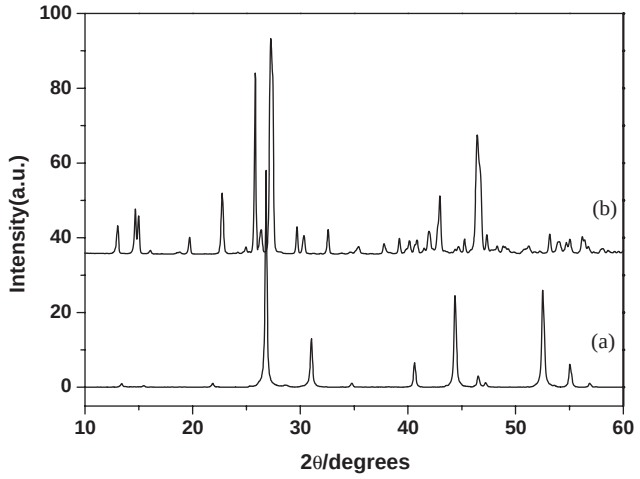

Fig. 2. X-ray powder diffraction patterns of (a) RbY_3F_{10}, and (b) RbY_2F_7.

Table 3
Correlation of cation size to the reaction products of rubidium rare-earth fluorides

Ln^{3+}	$r_{Rb}+/r_{Ln}3+$	Product	
La^{3+}	1.326	LaF_3	
Pr^{3+}	1.367	PrF_3	
Nd^{3+}	1.389	NdF_3	
Sm^{3+}	1.423	$SmF_3+RbSm_2F_7$	
Eu^{3+}	1.446	$RbEu_3F_{10}$	
Gd^{3+}	1.458	$RbGd_3F_{10}$	
Tb^{3+}	1.483	$RbTb_3F_{10}$	
Dy^{3+}	1.496	$RbDy_3F_{10}$	
Ho^{3+}	1.509	$RbHo_3F_{10}$	
Y^{3+}	1.515	RbY_3F_{10}	RbY_2F_7
Er^{3+}	1.535	$RbEr_3F_{10}$	$RbEr_2F_7$
Tm^{3+}	1.549	$RbTm_3F_{10}$	
Yb^{3+}	1.563		$RbYb_2F_7$
Lu^{3+}	1.577		$RbLu_2F_7$

R.D. The crystal ionic radii of the rare-earth cations were obtained from *Encyclopedia of Inorganic Chemistry*, 2, 929–941; R.B. King, Wiley, New York (1994).

in the range $1.42<R<1.55$. The small rare-earth cations with $R>1.51$ may lead to $RbLn_2F_7$ (Ln= Y, Er, Yb and Lu). It should be pointed out that the stable range of the cubic $RbLn_3F_{10}$ phases under hydrothermal condition is significantly wider than that obtained by high-temperature reaction, where the cubic $RbLn_3F_{10}$ were obtained only for Sm, Eu, Gd and Tb [5]. Smaller rare-earth cations may also form $RbLn_3F_{10}$ but in different structures, such as hexagonal [13] and orthorhombic [17] RbY_3F_{10}. It is known that the cubic $RbLn_3F_{10}$ is a low-temperature phase [8,13] and it transforms to hexagonal structure at high temperature. The hydrothermal synthesis favors the low-temperature cubic phase and, indeed, we have not observed the hexagonal $RbLn_3F_{10}$ in our study.

3.2. Luminescent properties of Eu^{3+}-doped $RbGd_3F_{10}$ and RbY_3F_{10}

Fig. 3 shows the excitation spectra of $RbGd_3F_{10}$:Eu^{3+} (0.5 mol%) (curve a) and RbY_3F_{10}:Eu^{3+} (0.5 mol%) (curve b). The broad excitation band centered at about 125 nm in the spectrum of RbY_3F_{10}:Eu^{3+} is assigned to the host absorption [18], while the broadband at 120 nm with stronger intensity in that of $RbGd_3F_{10}$:Eu^{3+} originates mainly from the $4f-5d$ transition of Gd^{3+} ions [16] and partly from the host absorption. The weak bands at about 160 nm in both spectra originate from the F–Eu^{3+} charge transfer (CT) transition [18]. The sharp excitation peaks in the spectrum of RbY_3F_{10}:Eu^{3+} (251–465 nm) originates from the transitions from the ground-state ^7F_J to the excited states ^5G_J, ^5H_J, ^5L_J and ^5D_J within the f^6 configuration of Eu^{3+} cations. The strongest sharp peak located at about 393 nm is assigned to the $^7F_0\rightarrow{}^5L_5$ transition of Eu^{3+}. For $RbGd_3F_{10}$:Eu^{3+}, the sharp excitation peaks originate from the transitions from the ground-state $^8S_{7/2}$ of Gd^{3+} to the excited states ^6G_J (195 and 202 nm), ^6D_J (244 and 252 nm), ^6I_J (274 nm) and ^6P_J (305 and 311 nm), respectively. Because of the low doping level of Eu^{3+} (0.5 mol%) and the efficient energy transfer from Gd^{3+} to Eu^{3+}, the $f\rightarrow f$ transitions of Eu^{3+} are very weak in the excitation spectrum of $RbGd_3F_{10}$:Eu^{3+}. In both materials, the $O^{2-}\rightarrow Eu^{3+}$ charge transfer transition, which should be a broadband at about 250 nm [19,20], does not appear in the excitation spectra, indicating that the oxygen content is very low in the fluorides obtained by hydrothermal technique.

In cubic $RbLn_3F_{10}$, the rare-earth atoms are located in square antiprismatic coordination. The local symmetry of the rare-earth atoms is noncentrosymmetric.

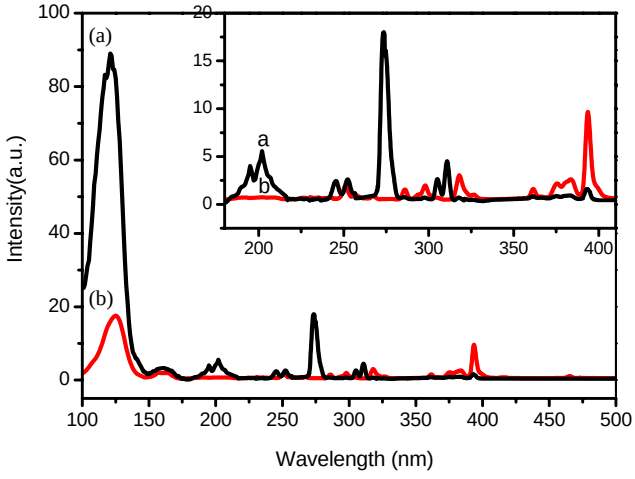

Fig. 3. Excitation spectra of (a) $RbGd_3F_{10}$:Eu^{3+} (0.5 mol%), and (b) RbY_3F_{10}:Eu^{3+} (0.5 mol%) for monitoring Eu^{3+} $^5D_0\rightarrow{}^7F_1$ emission intensity at 594 nm.

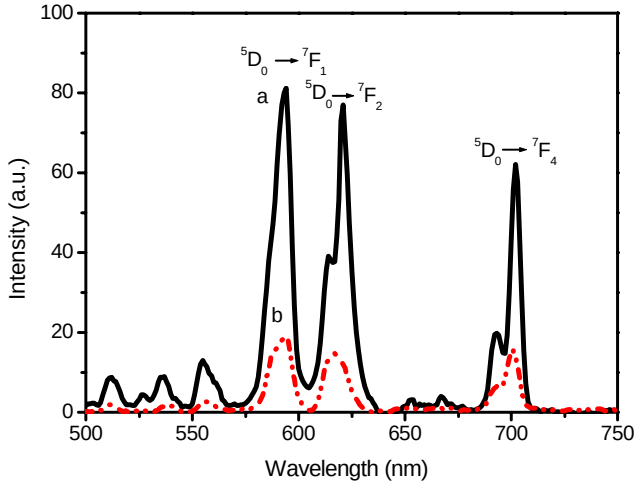

Fig. 4. Emission spectra of (a) $RbGd_3F_{10}:Eu^{3+}$ (0.5 mol%) upon excitation in the ^6I_J levels of Gd^{3+} at 274 nm, and (b) $RbY_3F_{10}:Eu^{3+}$ (0.5 mol%) upon excitation in the $^5L_5$ levels of Eu^{3+} at 393 nm.

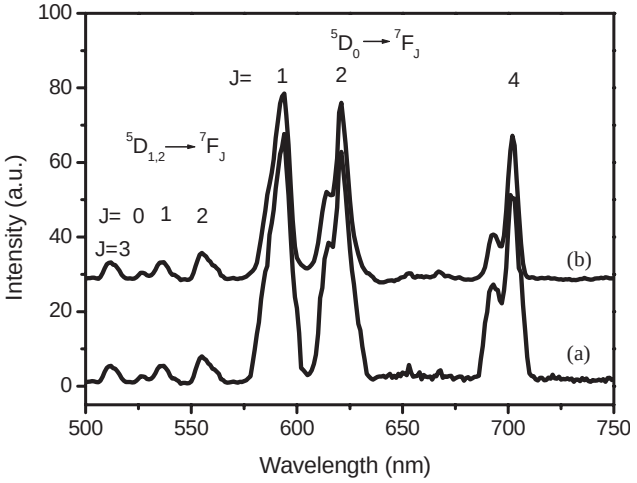

Fig. 5. Emission spectra of $RbGd_3F_{10}$: Eu^{3+} (0.5 mol%), (a) upon excitation in the ^6G_J level of Gd^{3+} at 202 nm, and (b) upon excitation in the ^6I_J level of Gd^{3+} at 274 nm (the spectra are scaled on the $^5D_1 \rightarrow {}^7F_2$ emission intensity).

Fig. 4 shows the emission spectra of $RbGd_3F_{10}:Eu^{3+}$ and $RbY_3F_{10}:Eu^{3+}$. It can be seen that the dominant emission transitions are $^5D_0 \rightarrow {}^7F_1$ (magnetic dipole–dipole transition) and $^5D_0 \rightarrow {}^7F_2$ (electric dipole–dipole transition), which agrees well with the crystal character of noncentrosymmetric sites occupied by rare-earth ions.

$RbGd_3F_{10}:Eu^{3+}$ also exhibits quantum cutting effect as that observed in $LiGdF_4:Eu^{3+}$ [2], which can be easily observed considering the emission spectra. Fig. 5 shows the emission spectra of $RbGd_3F_{10}:Eu^{3+}$ (0.5 mol%) upon excitation in the ^6G_J levels of Gd^{3+} at 202 nm and upon excitation in the ^6I_J levels of Gd^{3+} at 274 nm, respectively. The spectra are scaled on the $^5D_1 \rightarrow {}^7F_2$ emission intensity. It can be seen that the relative intensities of the emission from upper ^5D_J ($J = 1,2,3$) levels are stronger under the excitation in ^6I_J (274 nm) levels than that under excitation in ^6G_J (202 nm) levels, indicating the occurrence of the quantum cutting effect. Upon excitation in the ^6G_J levels of Gd^{3+}, the absorbed energy was transferred via a two-step cascade process to Eu^{3+}, resulting in two red photons. The energy of transitions $^6G_J \rightarrow {}^6P_J$ of Gd^{3+} match very well with that of $^7F_J \rightarrow {}^5D_0$ of Eu^{3+}; therefore, for the first step, energy is transferred by cross-relaxation, Gd^{3+} relaxes from the ^6G_J state to one of the ^6P_J states, exciting Eu^{3+} from the ^7F_J state to the $^5D_0$ state, resulting in a red emission photon from $^5D_0$ to ^7F_J. Gd^{3+} in the ^6P_J state transfers energy to Eu^{3+}, which is pumped up to the higher excited state of ^5D_J. The emission of the second photon is, therefore, composed of full spectrum of all $^5D_J \rightarrow {}^7F_J$ transitions. Accordingly, the quantum efficiency can be calculated with the formula proposed by Wegh et al. [2]:

$$\frac{P_{CR}}{P_{CR}+P_{DT}} = \frac{R(^5D_0/^5D_{1,2,3})_{^6G_J} - R(^5D_0/^5D_{1,2,3})_{^6I_J}}{R(^5D_0/^5D_{1,2,3})_{^6I_J}+1}, \quad (4)$$

where P_{CR} is the probability for cross-relaxation, and P_{DT} is the probability for the direct energy transfer from Gd^{3+} to Eu^{3+}, $R(^5D_0/^5D_{1,2,3})$ is the ratio of the $^5D_0$ and the $^5D_{1,2,3}$ emission intensities, and the subscript (^6G_J or ^6I_J) indicates the excitation level for which the ratio is obtained. The quantum efficiency obtained is about 150% for $RbGd_3F_{10}:Eu^{3+}$.

4. Conclusion

We demonstrated that the hydrothermal method was a promising technique for synthesis of rubidium and rare-earth fluorides. The oxygen content is very low in the products. Three phases, tetragonal LnF_3, cubic $RbLn_3F_{10}$ and hexagonal $RbLn_2F_7$, were obtained in the Rb–*Ln*–F systems under the present study. The large rare-earth cations (Ln= La−Nd) only form LnF_3, the small ones (Ln= Er, Yb, Lu and Y) form $RbLn_2F_7$, while $RbLn_3F_{10}$ was obtained for the in-between rare-earth cations (Ln= Eu−Tm, Y). All $RbLn_3F_{10}$ phases obtained by hydrothermal synthesis crystallize in the γ-KYb_3F_{10}-type structure. The downconversion energy transfer was observed in $RbGd_3F_{10}:Eu^{3+}$ (0.5 mol%) and the quantum efficiency is about 150% under the excitation in the ^6G_J level of Gd^{3+} ions.

Acknowledgments

This work was financially supported by the Natural Science Foundation of China under the project grant number 10204001 and partially supported by the Beijing Jiaotong University under the grant number 2002RC032. We are grateful to Prof. Xurong Xu and to Prof. Jianhua Lin for helpful discussions.

References

[1] C.R. Ronda, T. Jüstel, H. Nikol, J. Alloys Compd. 275–277 (1998) 669–676.
[2] R.T. Wegh, H. Donker, K.D. Oskam, A. Meijerink, Science 283 (1999) 663–666.
[3] O. Greis, J.M. Haschke, in: K.A. Gschneider (Ed.), Handbook on the Physics and Chemistry of Rare Earths, Vol. 5, North-Holland, Amsterdam, 1982, pp. 387–460.
[4] R.E. Thoma, Inorg. Chem. 1 (1962) 220–226.
[5] A. Vedrine, R. Boutonnet, R. Sabatier, J.C. Cousseins, Bull. Soc. Chim. Fr. 3–4 (1975) 445–448.
[6] Z.J. Kang, Y.X. Wang, F.T. You, J.H. Lin, J. Solid State Chem. 158 (2001) 358–362.
[7] J. Metin, R. Mahiou, M.T. Fournier, J.C. Cousseins, Mater. Res. Bull. 22 (1987) 1131–1136.
[8] J. Metin, R. Mahiou, C. Linares, M.T. Fournier, J. Alloys Compd. 206 (1994) 109–112.
[9] S. Aleonard, J. Solid State Chem. 42 (1982) 80–88.
[10] A. Vedrine, A. Delaigue, J.C. Cousseins, Rev. Chim. Miner. 11 (1974) 217–222.
[11] S. Aleonard, Y. Lefur, M.F. Gorius, M.T. Roux, J. Solid State Chem. 34 (1980) 79.
[12] S. Aleonard, O. Gonzales, M.F. Gorius, M.T. Roux, Mater. Res. Bull. 10 (1975) 1185–1192.
[13] M. Tachihante, M.T. Founier, A. Arbus, J.C. Cousseins, Solid State Commun. 51 (1984) 577–580.
[14] A. Ellens, S.J. Kroes, J. Sytsma, G. Blasse, Mater. Chem. Phys. 30 (1991) 127–133.
[15] Chunyan Zhao, Shouhua Feng, Ruren Xu, Chunsan Shi, Jiazhan Ni, Chem. Commun. (1996) 945–946.
[16] Fangtian You, Yingxia Wang, Jianhua Lin, Ye Tao, J. Alloys Compd. 343 (2002) 151–155.
[17] J. Chassaing, J. Inorg. Nucl. Chem. 37 (1975) 1554–1556.
[18] J.C. Krupa, M. Queffelec, J. Alloys Compd. 250 (1997) 287–292.
[19] N. Martin, P. Boutinaud, R. Mahiou, J.C. Cousseins, M. Bouderbala, J. Mater. Chem. 9 (1999) 125.
[20] A. Mayolet, J.C. Krupa, I. Gerard, P. Martin, Mater. Chem. Phys. 31 (1992) 107–109.